Journal of Nuclear Materials 456 (2015) 272–280

Contents lists available at ScienceDirect

Journal of Nuclear Materials

journal homepage: www.elsevier.com/locate/jnucmat

Transmission electron microscopy characterization of Zircaloy-4 and ZIRLO™ oxide layers

Benoit de Gabory [a,*], Arthur T. Motta [a], Ke Wang [b]

[a] Department of Mechanical and Nuclear Engineering, Penn State University, University Park, PA 16802, USA
[b] Materials Characterization Laboratory, Penn State University, University Park, PA 16802, USA

ARTICLE INFO

Article history:
Received 20 December 2013
Accepted 28 September 2014

ABSTRACT

Waterside corrosion of zirconium alloy nuclear fuel cladding varies markedly from one alloy to another. In addition, for a given alloy, the corrosion rate evolves during the corrosion process, most notably when the oxide loses its stability at the oxide transition. In an effort to understand the mechanism resulting in the variations of corrosion rate observed at the oxide transition, oxide layers formed on Zircaloy-4 and ZIRLO™ in high temperature water autoclave environments, and archived before and after the transition, are characterized using transmission electron microscopy.

The study characterizes and compares the oxide morphology in both alloys at different times during the corrosion process, in an effort to understand the oxide growth mechanism for these alloys. Results show that the oxide is mainly composed of monoclinic ZrO_2[1], with a preponderance of columnar oxide grains which extend to the oxide/metal interface. The oxide formed right after the transition has occurred, exhibits a 150 nm-wide layer of small equiaxed grains with high tetragonal oxide fraction. This layer has a similar morphology and structure as the first oxide layer formed (observed near the oxide/water interface). A study of the oxygen-rich region near the oxide/metal interface reveals a complex structure of different phases at different stages of corrosion. The interface exhibits an intermediate layer, identified as ZrO, a discontinuous layer of "blocky" Zr_3O grains embedded in the ZrO layer, and a suboxide layer corresponding to an oxygen saturated solid solution in the metal matrix side. The thickness of this interfacial layer decreased markedly at the transition.

Hydrides are also observed in that region, with a definite orientation relationship with the matrix. The observations of the oxide/metal interface are qualitatively similar for the two alloys but quantitatively different. The incorporation of intermetallic precipitates into the oxide layer is also studied, and compared between the two alloys.

These results are discussed in terms of previous observations and of current models of oxide growth.

1. Introduction

Zirconium-based alloys are widely used for nuclear fuel cladding because of their good mechanical behavior, resistance to corrosion, and low thermal neutron absorption cross-section. The corrosion behavior of these alloys is still under investigation, as a more complete understanding of corrosion kinetics can help design better alloys that can potentially sustain harsher conditions and longer fuel cycles.

The different corrosion rates observed in different zirconium alloys are thought to be related to the microstructure of the respective oxide layers formed in these alloys [1,2]. The microstructure is also related to the variations of the corrosion rate with exposure time that are presented in Fig. 1. In this context, a detailed characterization of this structure and interface between oxide and metal is key to a greater understanding of the corrosion mechanism, which could allow for alloy improvement.

Results obtained from transmission electron microscopy (TEM) samples archived just before and just after the first kinetic transition are presented here, and compared to previous transmission electron microscopy examinations of Zr alloy oxides [3–7]. From the ensemble of these observations and the variations of the microstructure at the transition, conclusions are drawn about the causes and consequences of the first kinetic transition in zirconium alloys.

* Corresponding author. Tel.: +1 814 206 6584.
E-mail address: benoit.degabory@gmail.com (B. de Gabory).

[1] We note that the observation of stress-stabilized tetragonal grains is made difficult by the alteration of the stress state of the oxide during TEM sample preparation, so it is possible that the tetragonal fraction is smaller in these samples than in the bulk oxide.

http://dx.doi.org/10.1016/j.jnucmat.2014.09.073
0022-3115/

2. Experimental procedures

2.1. Studied samples

Zircaloy-4 and ZIRLO™ recrystallized sheet samples were autoclave corroded in 360 °C pure water at saturation pressure at Westinghouse Electric Company in their laboratory facility in Churchill, PA. The Zircaloy-4 composition is Zr–1.45Sn–0.2Fe–0.1Cr (the alloying contents are indicated in weight percent). The composition of ZIRLO™ is Zr–1.0Sn–1.0Nb–0.1Fe. The processing of these alloys can be found in Ref. [8].

Fig. 1 shows the oxidation kinetics of the two alloys, determined by measuring the weight gain that results from oxygen ingress. The periodic behavior characteristic of the corrosion of Zr alloys is observed, with two marked transitions clearly visible for each alloy. Coupon samples were archived at different corrosion times for examination. For each alloy, three samples were selected from oxide layers formed in samples archived just before and just after the first oxide transition, as indicated by the arrows in Fig. 1. The exact exposure times and oxide thicknesses (determined from weight gain data) for the examined samples are shown in Table 1.

2.2. Sample preparation

From the selected samples, electron-transparent foils were prepared using the Focused Ion Beam (FIB) in-situ lift-out technique, using a FEI Quanta 3D 200, instrument operated at 30 keV, with currents between 30 pA and 7.0 nA. The lift-out method consists of extracting a thin foil from the sample, attaching it to a copper grid, and thinning it down even more to reach electron transparency (~100 nm thickness). This technique provides homogeneously-thinned TEM samples, taken from precise locations, e.g. close to the oxide/metal interface, and with large transparent areas to study. From each zirconium alloy bulk sample many such foils were extracted, so that detailed information could be obtained.

Examinations were performed in a JEOL 2010 TEM and a JEOL 2010F Scanning Transmission Electron Microscope (STEM) (for Electron Energy Loss Spectroscopy (EELS) measurements) at the Materials Characterization Laboratory at Penn State. These microscopes operate at 200 keV and are both equipped with a Gatan GIF spectrometer. Some Energy Dispersive Spectroscopy results were also obtained using a FEI TITAN 3G2 operated at 300 keV, equipped with a super-X detector.

3. Experimental results

3.1. Oxide morphology

Many TEM studies of Zr alloys oxide morphology have been previously performed, e.g. see [3,5,7]. We compare our results to the models explaining the oxide growth and precipitate oxidation mechanisms.

The six samples studied – pre- and post-transition – have an oxide thickness in the 2–3 μm range for Zircaloy-4, and 3–4 μm range for ZIRLO™, approximately (see Table 1). On a single TEM sample prepared as described above (thin area of about 8 × 10 μm), the entire thickness of the oxide layer can be seen, as well as the metal ahead of the oxide/metal interface, allowing for a comprehensive examination.

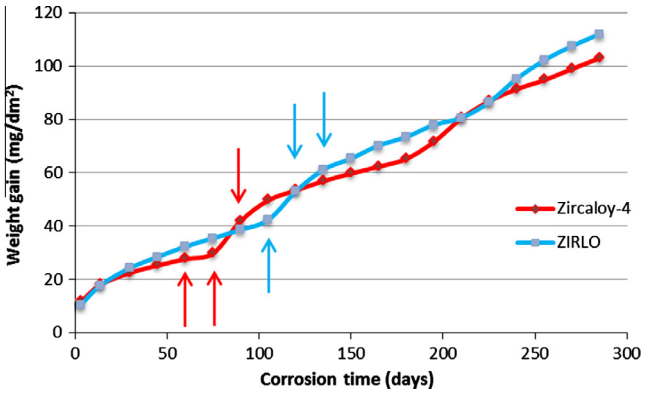

Fig. 1. Corrosion weight gain versus exposure time in 360 °C water for ZIRLO™ and Zircaloy-4; studied samples are arrowed.

In the oxide formed on the two alloys, both large columnar grains and smaller equiaxed grains are observed. The latter are more prevalent near the oxide/water interface and in the regions surrounding cracks in the oxide. Whether the cracks cause the smaller oxide grains or whether the region near the grains is more easily cracked during sample preparation is not clear. Large lateral cracks are observed mainly parallel to the oxide/metal interface.

Successive bright-field micrographs were taken in the post-transition Zircaloy-4 sample (oxidized for 90 days to an oxide thickness of 2.8 μm), going deeper into the oxide layer, in order to study the evolution of the oxide morphology formed before and after the transition. These micrographs were assembled to present a comprehensive picture of the oxide morphology, as shown in the upper part of Fig. 2. Detailed observation of the micrographs allowed to manually trace the oxide grain boundaries, to more clearly highlight the grain morphology (bottom part of Fig. 2). Columnar grains can be observed, aligned in the oxide growth direction and growing perpendicular to the oxide/metal interface and extending up to the oxide/metal interface itself.

By calculating the weight gain since the transition (14.7 mg/dm^2 ≡ 1 μm) and taking that distance (11.9 mg/dm^2 ~ 800 nm for the post-transition Zircaloy-4 sample, see Table 2) from the oxide/metal interface, the oxide location where the transition occurred can be found. The oxide formed at the transition corresponds to a layer of equiaxed grains, with diameter close to the columnar grain width. The layer is easy to identify in bright-field imaging because of the in-plane cracks going through it. This layer is about 150 nm wide, and was observed in both alloys.

The oxide grains in the two alloys were measured, and an average length and width calculated from about 150 grains, to compare with previous results [3,7]. The ZIRLO™ oxide grains are larger and

Table 1
Exposure time, measured corrosion weight gain and calculated oxide thickness for the ZIRLO™ and Zircaloy-4 studied samples.

		Exposure time (days)	Weight gain (mg/dm^2)	Oxide thickness (μm)
Zircaloy-4	Pre-transition	60	27.7	1.9
		75	29.8	2.0
	Post-1st transition	90	41.7	2.8
ZIRLO™	Pre-transition	105	42.3	2.9
	Post-1st transition	120	52.7	3.6
		135	61.2	4.2

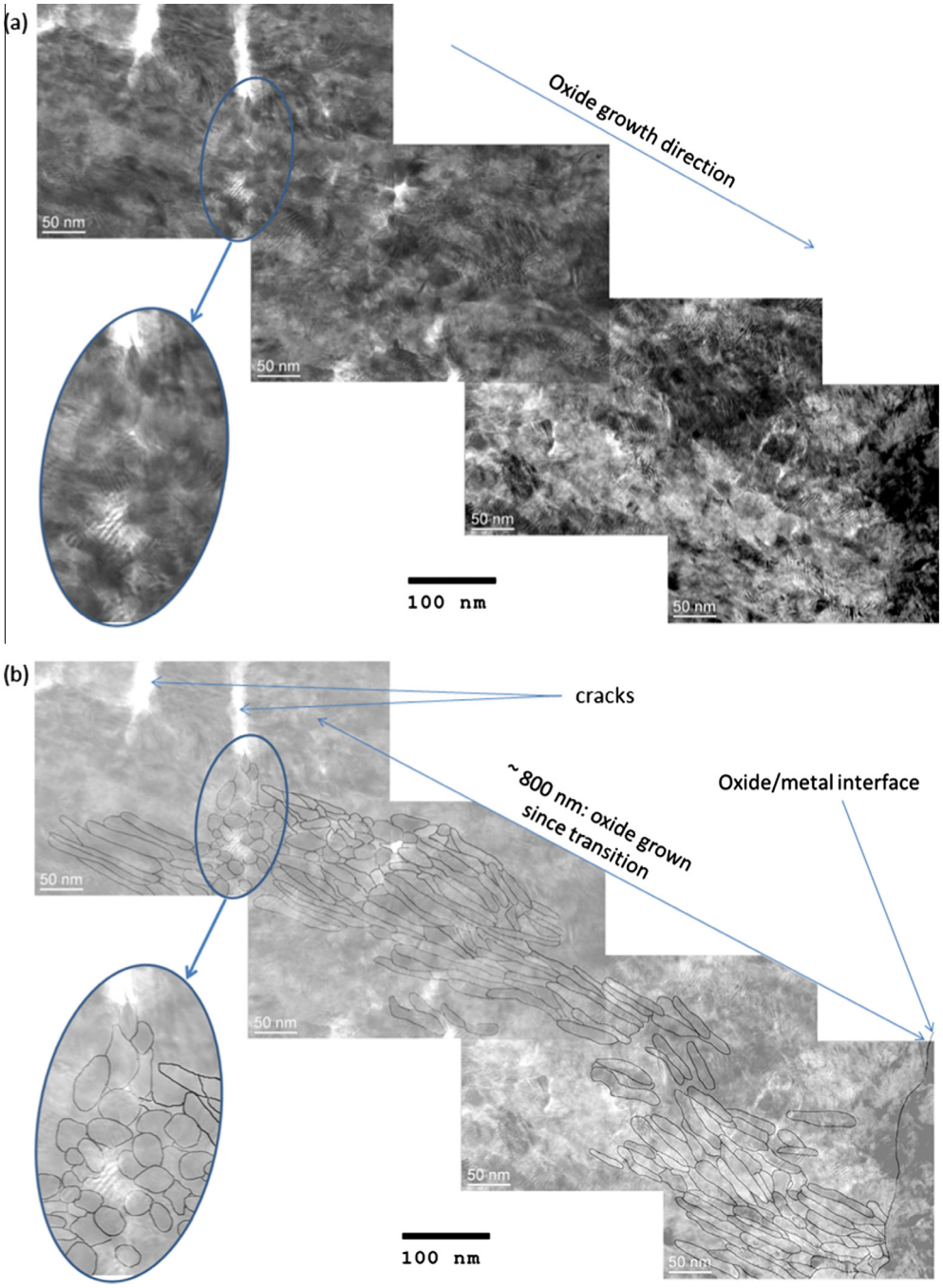

Fig. 2. (a) Bright-field microscopy showing oxide structure; (b) outlined morphology of the oxide grains grown after transition.

Table 2
Measured grains size and aspect ratio for the oxide grown on ZIRLO™ and Zircaloy-4.

		Zircaloy-4	ZIRLO™
Columnar grains	Width range (nm)	10–40	15–45
	Average width (nm)	20	30
	Length range (nm)	80–300	130–340
	Average length (nm)	140	200
	Aspect ratio range	4–12	4–10
	Average aspect ratio	7	7.5
Equiaxed grains	Diameter range (nm)	10–25	15–30
	Average diameter (nm)	15	25

longer than those in Zircaloy-4, but with the same aspect ratio, as shown in Table 2. Wider grains have been previously reported to be associated with better corrosion resistance [3]. The average aspect ratio (length/width) is close to 7 for both alloys, and ranging between 4 and 12.

The oxide grown after the transition exhibits a similar structure as that grown before transition. The only impact of transition on the oxide morphology appears to be that the oxide grains formed during the transition are predominantly equiaxed, in good agreement with the periodic nature of the corrosion process, and with the oxide growth mechanism.

The columnar grains observed in Zircaloy-4 each react differently to tilt in the TEM, when imaged in bright-field, as a consequence of the strong grain-to-grain misorientation. This misorientation is quantitatively seen to be more significant in Zircaloy-4 oxide than in ZIRLO™ oxide, as observed previously [3].

3.2. Second-phase particles

3.2.1. Zircaloy-4

The second-phase particles found in Zircaloy-4 are $Zr(Fe,Cr)_2$ precipitates, which exhibit the Laves phase C-14 (hexagonal) structure, as determined by diffraction analysis. These precipitates are often faceted, with a length between 100 and 250 nm, and show stacking faults. The precipitates are incorporated into the oxide in their metallic state and only oxidize after a certain distance from the oxide/metal interface [6]. Fig. 3 shows three bright-field micrographs of $Zr(Fe,Cr)_2$ precipitates observed in a pre-transition Zircaloy-4 sample, in the metal (a), incorporated unoxidized in the oxide layer (b) and oxidized (c) further into the oxide layer.

For the incorporated metallic second-phase particles, a crack is often observed on the side of the precipitate opposite to the interface, as seen in [3,9]. While the precipitate remains unoxidized (and its volume does not change), the matrix around it keeps oxidizing and expands in the oxide growth direction, leading to the formation of a crack on top of the precipitates [6].

In Zircaloy-4, oxidized $Zr(Fe,Cr)_2$ precipitates appear as a collection (about the size of the unoxidized precipitates – e.g. a diameter about 100–200 nm) of small equiaxed grains with a diameter on the order of 10 nm, separated by small cracks. Fig. 4(a) shows a bright-field micrograph taken from an oxidized precipitate located about 800 nm from the oxide/metal interface of a Zircaloy-4 sample archived before transition. Fig. 4(b) shows a diffraction pattern taken from the oxidized precipitate, exhibiting a high intensity of tetragonal oxide peaks, in good agreement with previous studies associating small equiaxed grains with the tetragonal phase [3]. The stabilization of the tetragonal phase can be explained by the high concentration of alloying elements, the small grain size and possibly the stresses created by the delayed volume expansion of the precipitate compared to the oxide matrix.

3.2.2. ZIRLO™

Two different types of second-phase particles are observed in ZIRLO™ samples. The first type are ZrFeNb particles, exhibiting a C14 Laves phase structure (similar to the structure of $Zr(Fe,Cr)_2$ precipitates). These precipitates have similar morphology as the Zircaloy-4 Laves phase precipitates, i.e. they are faceted, 75–200 nm long, and show stacking faults. The second type are β-Nb precipitates, that are roundish and smaller in size (~50–80 nm in diameter), and which contain no Fe. Fig. 5 shows a bright-field micrograph taken in the metal region near the oxide/metal interface of a ZIRLO sample, where the two types of precipitates are indicated: β-Nb are circled in black, ZrFeNb in white. In this micrograph, we can see β-Nb precipitates are found in greater number than the ZrFeNb particles. This is true both in the metal and in the oxide.

Both types of precipitates are incorporated in the oxide in metallic form, and the incorporated precipitates exhibit a crack on the side opposite to the oxide/metal interface. The difference with Zircaloy-4 is that when ZIRLO™ precipitates oxidize, they become amorphous. Amorphous precipitates show a "milky" appearance in bright field, exhibit an amorphous diffraction ring, and show no reaction to tilting. EDS measurements of the oxygen content, taken from the amorphous precipitates, show that these are oxidized. The oxidized precipitates show no crack on top. Fig. 6 is a bright-field micrograph taken from the bulk of the oxide

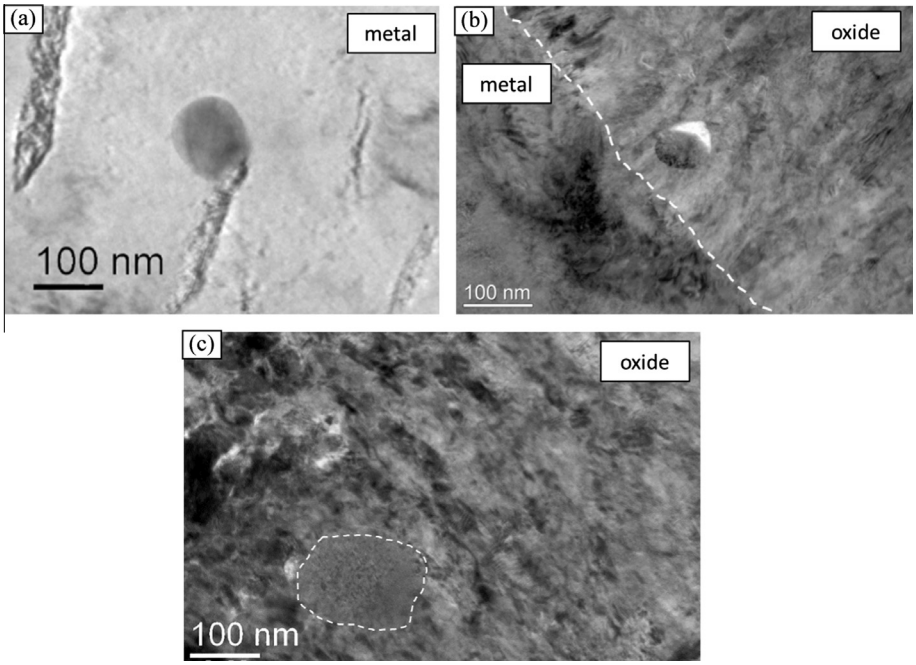

Fig. 3. (a) Second-phase particle in the Zircaloy-4 metal, (b) crystalline second-phase particle in the oxide layer and (c) oxidized second-phase particle.

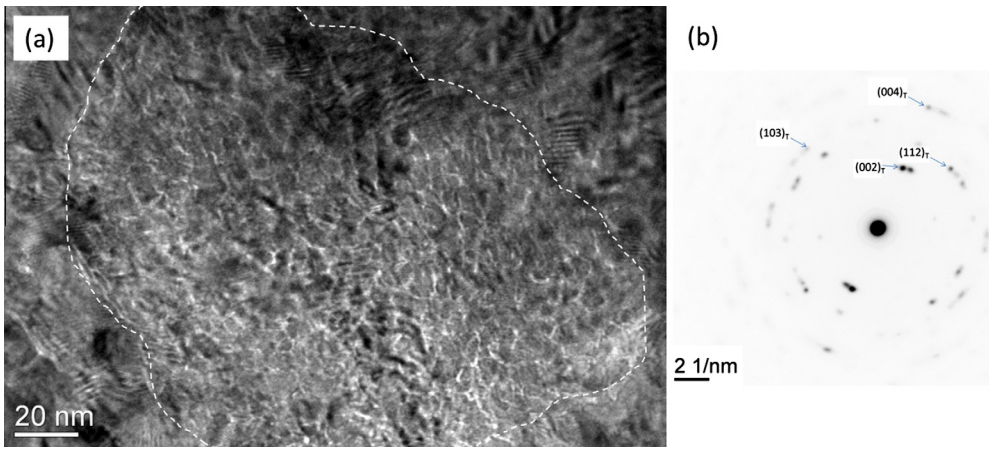

Fig. 4. (a) Oxidized second-phase particle structure and (b) associated diffraction pattern exhibiting tetragonal reflections.

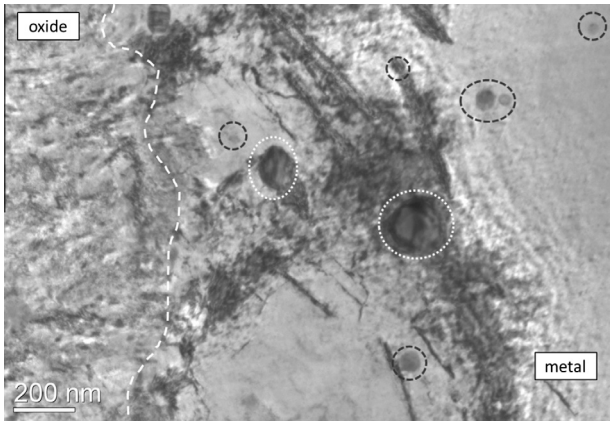

Fig. 5. Precipitates in the metal part of a ZIRLO™ sample. β-Nb are circled in black, ZrFeNb in white.

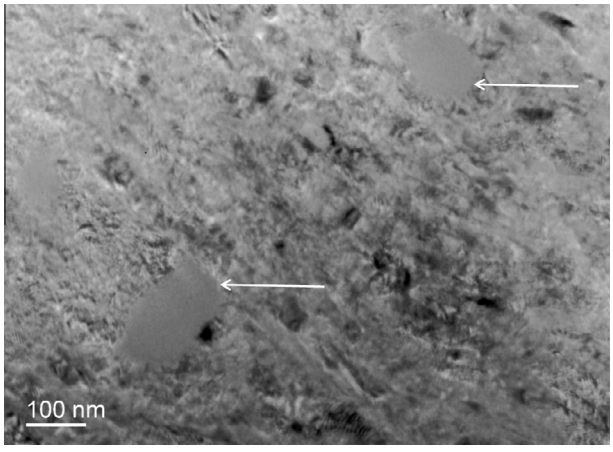

Fig. 6. Amorphous ZrFeNb precipitates in the bulk of the oxide layer grown on a ZIRLO™ sample archived just after transition.

(about 2.0 μm from the oxide/metal interface) of a ZIRLO™ sample archived just after the transition. The morphology of two amorphous ZrFeNb precipitates can be observed on this micrograph.

An Energy Dispersive Spectroscopy (EDS) analysis of the incorporated precipitates has been performed, and the chemical content was obtained from the EDS spectrum using a Cliff–Lorimer quantification model. Fig. 7(a) shows a High Angle Annular Dark Field micrograph taken near the oxide/metal interface of a pre-transition ZIRLO™ sample. Precipitates appear clearly, and their chemical composition can be identified on the EDS map presented in Fig. 7(b): the circled precipitates contain no Fe, and are β-Nb, while the others contain both Nb and Fe, and are ZrFeNb precipitates.

Quantitatively, the analysis shows that metallic β-Nb precipitates contain about 80 at.% Nb and 20 at.% Zr. When β-Nb precipitates oxidize, the amount of Zr they contain increases significantly – although the increase could be explained by matrix interference, given the small size of the precipitates. The five ZrFeNb precipitates measured had a Nb/Fe ration around 2. After incorporation, the chemical composition did not vary significantly (for precipitates located as far as 450 nm away from the interface).

The ZrFeNb precipitates appear to remain unoxidized longer in the oxide than the smaller β-Nb precipitates: amorphous β-Nb precipitates have been observed as close as 400 nm from the oxide/metal interface, while the closest amorphous ZrFeNb precipitate observed was found 700 nm away from it. The amorphization distance of β-Nb precipitates is shown in the three bright-field micrographs taken along the oxide/metal interface of a ZIRLO™ sample oxidized for 120 days, and assembled to provide a comprehensive picture presented in Fig. 8. Many precipitates were observed, in majority β-Nb precipitates indicated in white (metallic precipitates) and gray (three amorphous precipitates). Only one ZrFeNb metallic precipitate could be seen in these micrographs, indicated in black, and no amorphous ZrFeNb was observed. Large amorphous precipitates – of the ZrFeNb type – have been observed up to the oxide/water interface.

3.3. Hydrides

Hydrides are often observed in the metal layer close to the oxide/metal interface. The observed hydrides exhibit an elongated morphology, measuring around 150–300 nm in length and about 40–60 nm in width, with little differences in size between the two alloys. Fig. 9 shows a HAADF taken from the oxide/metal interface of an oxide formed on a Zircaloy-4 sample after a 75 day exposure. Below the oxide/metal interface, indicated by the white dotted line, elongated particles can be observed. These particles were positively identified as delta hydrides by electron diffraction. The elongated morphology is in good agreement with previous TEM observations of hydrides in Zircaloy-4 [10]. Most of the hydrides are oriented roughly parallel to the oxide/metal interface, although some of them are closer to the interface normal direction.

In the pre-transition ZIRLO™ sample, long hydrides can be observed, with a length between 3 and 5 μm. Although these long hydrides have only been observed in this sample, they have been reported by previous studies [10]. The orientation relationship

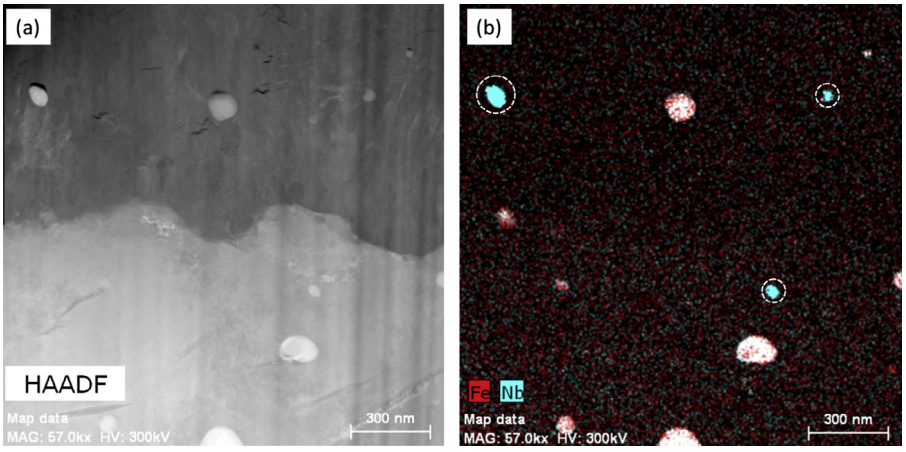

Fig. 7. (a) High Angle Annular Dark Field picture of the interface, exhibiting precipitates in the metal and in the oxide layer. (b) EDS mapping showing Nb in blue and Fe in red. ZrFeNb precipitates appear white, while β-Nb precipitates are circled by white dotted lines. (For interpretation of the references to color in this figure legend, the reader is referred to the web version of this article.)

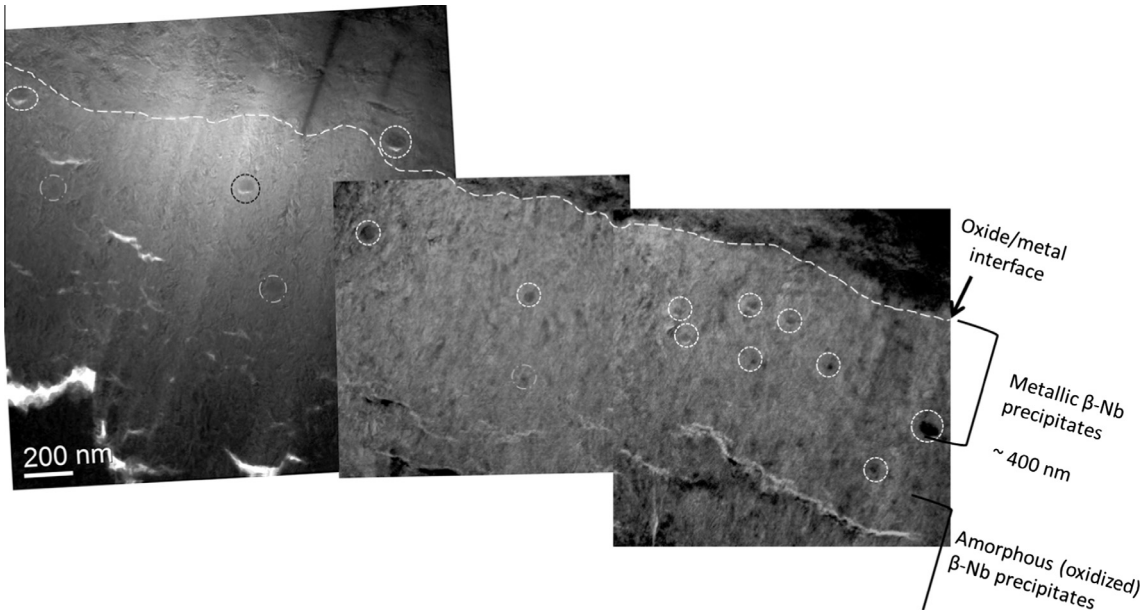

Fig. 8. Precipitates found in a post transition ZIRLO™ oxide. The white line shows the oxide grown since the onset of transition. Metallic β-Nb are circled in white, metallic ZrFeNb in black, and oxidized β-Nb in gray (different dotted line).

between the hydrides and the crystal matrix was characterized for the zone axis $[\bar{1}2\bar{1}]$ and $[\bar{1}100]$, respectively:

$(0002)_\alpha // (111)_{ZrH2}$ and $(11\bar{2}0)_\alpha // (202)_{ZrH2}$

Fig. 10 shows the details of the orientation relationship characterization: (a) shows the indexed diffraction pattern taken from a region containing the hydrides and the surrounding matrix. This diffraction pattern exhibits the relationship between the orientation of the matrix and the orientation of the hydrides presented above. A dark-field micrograph (b) was taken using the hydride spot indicated by the arrow and compared to the bright-field micrograph taken from the metal of the pre-transition ZIRLO™ sample (c). Comparing (b) and (c) confirms the indexing of the hydride spots. The same confirmation was performed for the matrix spots.

3.4. Oxide/metal interface

Bright-field micrographs show a thin intermediate layer along the oxide/metal interface, between the newly formed oxide grains and the metal. This layer has been observed in both alloys, in samples before and after transition. Its thickness varies from sample to sample, but for all studied alloys, there is a significant decrease of the intermediate layer thickness between the pre- and post-transition samples. Fig. 11(a) and (b) are bright-field micrographs taken from the oxide/metal interface of a pre- and a post-transition Zircaloy-4 sample, respectively. In each case, the intermediate layer is indicated by the arrows. The decrease of the intermediate thickness at transition can be seen by comparing the two micrographs.

For Zircaloy-4, a layer of thickness up to 60–75 nm has been observed in the sample just before transition, while the thickness of the layer observed in the post-transition sample is on the order of 5–10 nm. For ZIRLO™, the same layer is observed before transition, but wider – in the order of 60–90 nm – with greater variations in the thickness along the oxide/metal interface than observed in Zircaloy-4. In post transition ZIRLO™ samples, this layer is about 5 nm wide.

In a pre-transition Zircaloy-4 sample, some indications of discontinuity of the intermediate layer were observed in bright-field

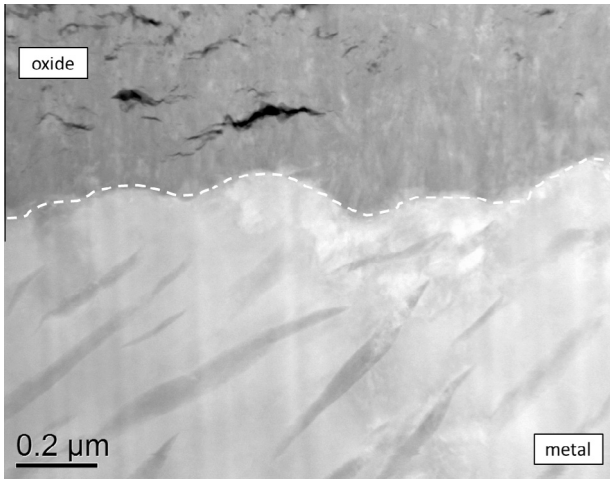

Fig. 9. Hydrides observed in the metal layer of a Zircaloy-4 sample, using High Angle Annular Dark Field to enhance the contrast.

imaging, and confirmed by EELS scans, but could not be related to any characteristic feature in the metal or the oxide.

Electron diffraction patterns taken from this layer are consistent with cubic ZrO, with lattice parameter $a = 0.46258$ nm (PDF #51-1149). Fig. 11(c) shows a diffraction pattern taken from the intermediate layer at the oxide/metal interface of a pre-transition ZIRLO sample, with the above index superimposed on the pattern. A similar ZrO phase was reported at the oxide/metal interface of a Zircaloy-4 sample in a X-ray diffraction study by Furuta [11], although with a smaller lattice parameter of 0.45848 nm. The presence of an equiatomic phase at the oxide/metal interface has also been reported using Atom Probe Tomography by Hutchinson et al. [12] in Zircaloy-2, Ni [4] in Zircaloy-4 and ZIRLO, and more recently on one of the Zircaloy-4 samples we studied, by Dong et al. [13]. Previous EELS scan measurements characterizing the oxygen content in the intermediate layer show that this layer contains about 45–55 at.% oxygen [14].

In several locations along the oxide/metal interface, "blocky" grains can be seen, interrupting the continuity of the intermediate layer. These grains appear darker under some tilt conditions, making

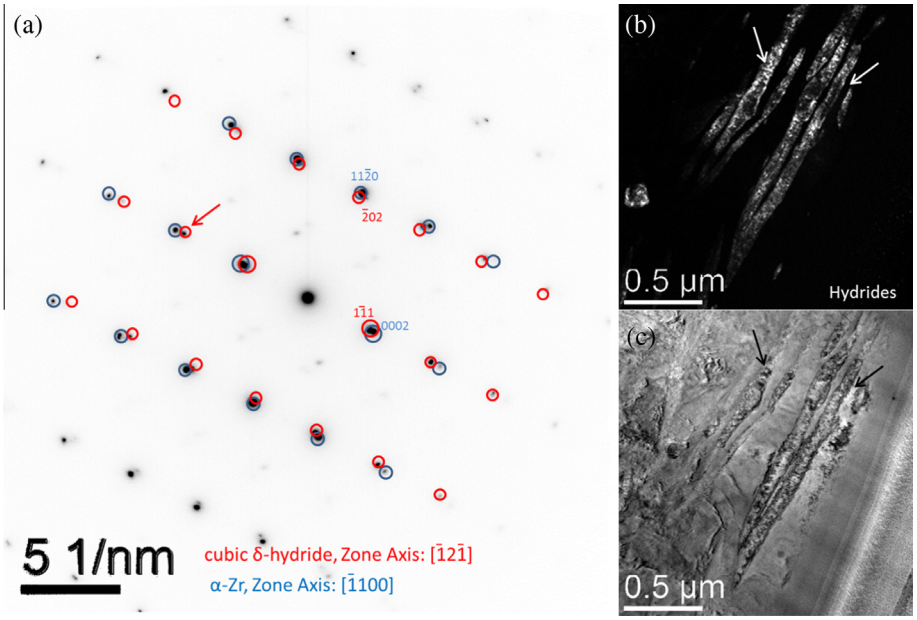

Fig. 10. (a) Orientation relationship hydride-matrix: indexed diffraction pattern, (b) dark-field micrograph taken from the hydride spot $(\bar{2}2\bar{2})$ indicated by the arrow in (a), and bright-field micrograph for comparison (c). The arrows in (b) and (c) correspond to the same location.

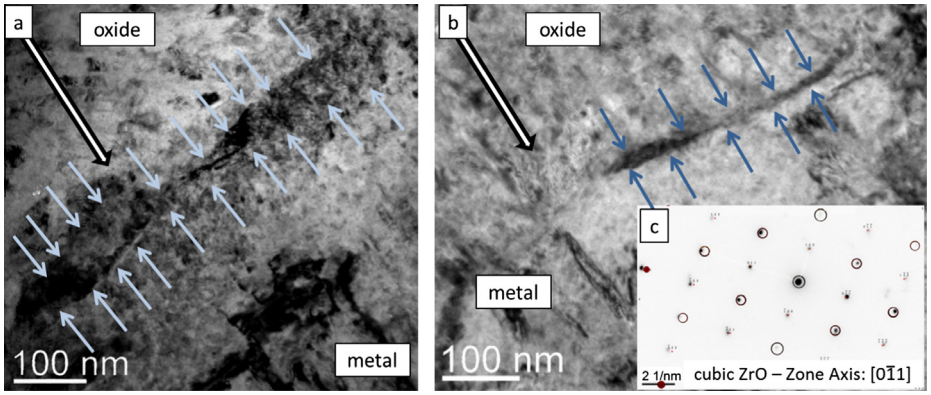

Fig. 11. Intermediate layer observed on pre- (a) and post-transition (b) Zircaloy-4 samples. The oxide growth direction is indicated by the big arrow. (c) Indexed electron diffraction pattern identifying the layer as cubic ZrO.

them relatively easy to identify. Fig. 12 is a bright-field micrograph taken from the oxide/metal interface of a pre-transition Zircaloy sample, where the blocky grains (arrowed) appear as faceted shapes at the oxide/metal interface, standing out from both the oxide and the metal layer. Their length is in the order of 80–100 nm, and there seems to be no preferential orientation of those grains along the oxide/metal interface.

The diffraction patterns taken from the blocky grains are consistent with rhombohedral Zr_3O (PDF #22-1025). This result is in agreement with the results presented in earlier studies [4] that have detected diffraction patterns from the rhombohedral Zr_3O structure at the interface.

In pre-transition samples, the region in the metal near the oxide/metal interface exhibits a different color and reaction to tilting than the metal grain. Fig. 13(a) is a bright-field micrograph taken from the oxide/metal interface of a pre-transition Zircaloy-4 sample, where a different layer can be seen ahead of the oxide.

The EELS measurements show that this region is oxygen-saturated, with about 30–35 at.% of oxygen in solid solution [14]. This "suboxide" region is about 150–200 nm wide in pre-transition Zircaloy-4 oxide samples, but could not be observed in the Zircaloy-4 post-transition sample. In the pre-transition ZIRLO™ oxide sample, it has a thickness comparable to that observed in the pre-transition Zircaloy-4 samples, i.e. on the order of 150–200 nm. In the post-transition ZIRLO™ sample archived after 120 days, it can be seen only at some places along the oxide/metal interface, while in the post-transition ZIRLO™ sample archived after 135 days, it could not be observed.

The diffraction patterns taken in the suboxide layer are consistent with a "distorted" α-Zr phase. This distortion could be induced by the high oxygen content in solid solution. Some electron diffraction patterns were consistent with the ω-Zr phase, metastable distortion of the α-Zr phase that has been observed in several alloys of Zr [4,15]. Fig. 13(b) is a diffraction pattern consistent with the ω-Zr phase, with the indexing superimposed.

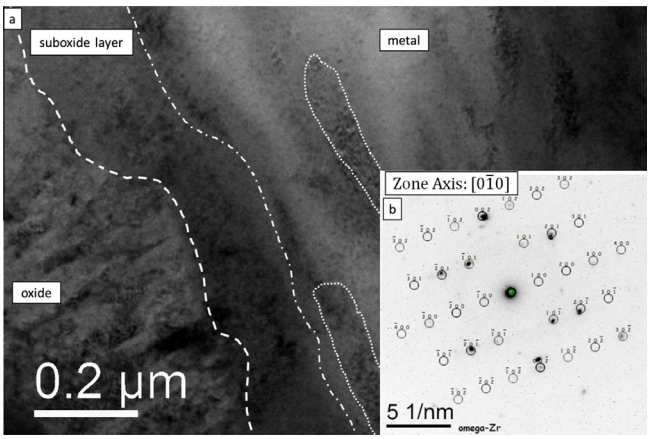

Fig. 13. (a) Layer in the metal near the oxide metal interface of a pre-transition Zircaloy-4 sample. Some hydrides are also visible in the metal. (b) Indexed electron diffraction pattern identifying the layer as ω-Zr.

4. Discussion

As a summary, observations of the oxide/metal interface revealed the presence of three different characteristic structural features:

- A thin (10–60 nm for Zircaloy-4, 15–90 nm for ZIRLO™) intermediate layer between oxide and metal, containing between 45 and 55 at.% oxygen.
- Blocky grains (80–100 nm wide) disrupting the continuity of this intermediate layer.
- A suboxide layer in the metal side of the interface (150–200 nm wide); its boundary with the metal is not as clear as those of the thin intermediate layer, and it contains between 35 and 30 at.% oxygen. This layer has not been observed in post-transition Zircaloy-4 samples, and has been observed only discontinuously in the ZIRLO™ sample archived during the transition (present in some places along the interface, not in others), and not at all in the post-transition ZIRLO™ sample.

The oxide transition has been proposed to be caused by a combination of porosity development and gradual stress accumulation during oxide growth leading to lateral cracking and interconnection of the existing porosity and easy access of the water to the oxide metal interface with a consequent increase in corrosion rate [8].

Previous studies [8] concluded that the oxide is initially formed as small equiaxed grains, with a comparatively high percentage of tetragonal ZrO_2 grains likely stabilized by small grain size. This is in good agreement with the observation of equiaxed grains near the oxide–water interface. Columnar grains then develop by self-selection from those small equiaxed grains. The oxide texture is oriented so as to minimize the stress accumulation during oxide growth, which translates into an overall fiber texture of columnar monoclinic oxide grains oriented such that the 200_M plane (orientation defined using the monoclinic zirconia Power Diffraction File #37-1484) is parallel to the oxide–metal interface.

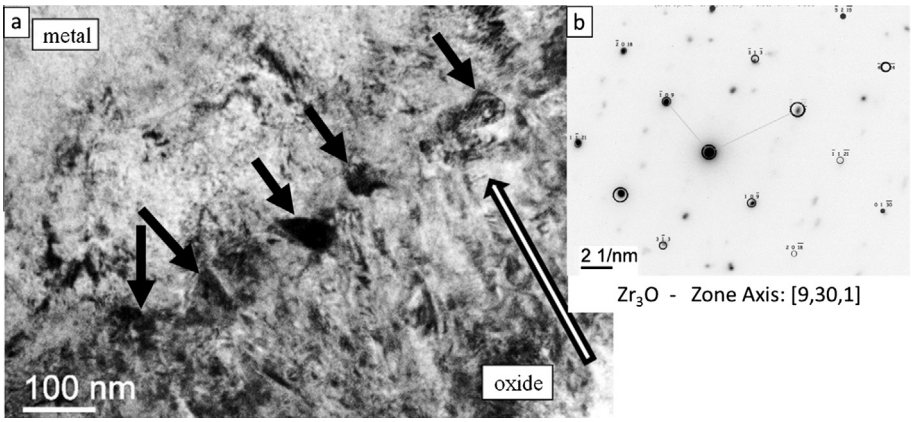

Fig. 12. (a) Blocky grains at the oxide metal interface of a pre-transition Zircaloy-4 sample, arrowed in black. Oxide growth direction indicated by the bigger arrow. (b) Indexed electron diffraction pattern identifying the grains as Zr_3O.

The observation of the state of oxidation of $Zr(Fe,Cr)_2$ second-phase particles in the oxide should be placed in context of previous studies of precipitate incorporation in the oxide layer [16]. This study reported that up to a certain distance from the oxide/metal interface the precipitates were incorporated in metallic form into the oxide layer formed on Zircaloy 4. Further away from the interface the Cris oxidized and the Fe appears as bcc agglomerates. Even further away completely oxidized precipitates are seen. It appears that similar observations can be applied to ZIRLO™ except that the oxidized precipitates appear amorphous instead of polycrystalline as seen in Zircaloy 4. Recent studies have indicated that hydrogen pickup during corrosion may be connected to the oxidation state of alloying elements in the oxide layer [17].

The observation of smaller oxide grains in Zircaloy-4 than in ZIRLO™ is consistent with the above picture since porosity develops at oxide grain boundaries and smaller oxide grains should lead to greater oxide porosity. Further, the observed greater degree of misorientation in the oxide formed on Zircaloy-4 than in ZIRLO™ would be in agreement with this mechanism as porosity would be more likely to develop on higher-angle grain boundaries than in well aligned grains.

The detailed observations of the metal region close to the oxide–metal interface may help clarify some of the previous observations. The presence of a layer of suboxide with a composition ~30% is in broad agreement with the phase diagram of Zr–O which predicts a 30% solid solution of oxygen in Zr in equilibrium with ZrO_2. The observation of Zr_3O is in agreement with previous synchrotron radiation observations and possibly with previous reports of the omega phase (it is difficult to distinguish between the reflections of these two phases). Finally a cubic ZrO phase (PDF #51-1149), likely metastable (not predicted in the Zr–O phase diagram), was observed at the oxide/metal interface, in good agreement with previous atom probe studies [4,12,13,18].

5. Conclusions

A detailed transmission electron microscopy study using FIB-prepared samples was conducted to characterize the structures of oxides formed in Zircaloy-4 and ZIRLO™, and their relationship to the corrosion kinetics and the oxide kinetic transition. The main conclusions are as follows:

- The oxide layer is predominantly composed of columnar grains, with some equiaxed grains found near cracks, near the oxide water interface (where the first oxide is formed), and in regions oxidized during the kinetic transition. A higher tetragonal ZrO_2 content is associated with the small grains.
- The intermetallic precipitates are incorporated into the oxide in metallic form and later become oxidized. In Zircaloy-4, the oxidized Laves phase precipitates are observed as a collection of small tetragonal oxide grains with extensive cracking. In ZIRLO™, Laves phases and small β-Nb precipitates become amorphous upon oxidation, about 400–500 nm from the oxide/metal interface (distance varying with precipitate size).
- Hydrides are found in the metal of both alloys, in an elongated columnar form, and aligned mostly parallel to the oxide/metal interface. Longer hydrides were observed in ZIRLO™, and identified as δ-hydrides, with an orientation relationship with the matrix:

$$(0002)_\alpha // (111)_{ZrH2} \text{ and } (11\bar{2}0)_\alpha // (202)_{ZrH2}$$

A characterization of the oxide/metal interface has also been conducted, with the two alloys showing similar results:

- Three different features at the oxide/metal interface are seen in the pre-transition oxide: (i) a small intermediate layer, identified as a cubic ZrO phase; (ii) blocky grains found at some places along the interface, with diffraction patterns indexed as Zr_3O; (iii) an oxygen-saturated suboxide layer in the metal.
- The width of these interfacial regions decreases at transition. The intermediate layer is smaller than before transition (10 nm, compared to 50 nm in the case of Zircaloy-4, 25 nm compared to 80 nm for ZIRLO™). The suboxide layer width decreases as well. The high corrosion rates at transition consume these layers, which start to develop again as the corrosion rate falls in the post transition regime.
- There are variations of this structure along the oxide/metal interface: in some places in the ZIRLO™ sample archived during the transition, the structure did not look like it was affected by transition; one pre-transition Zircaloy-4 sample showed indications of discontinuity, with both bright-field imaging and EELS oxygen profile.

Acknowledgements

The authors would like to thank Trevor Clark and Josh Maier for their valuable and expert assistance and advice regarding the TEM and the FIB. This work has been made possible thanks to the variety of oxidized samples provided by Robert Comstock at Westinghouse, as part of the MUZIC-2 program. This research was supported by a DOE NEUP Grant under Program Number NE0000315.

References

[1] H.-J. Beie, A. Mitwalsky, F. Garzarolli, H. Ruhmann, H.-J. Sell, in: 10th International Symposium on Zr in the Nuclear Industry, Baltimore, ASTM STP 1245, 1993, pp. 615–643.
[2] D. Pecheur, J. Godlewski, P. Billot, J. Thomazet, in: 11th International Symposium on Zr in the Nuclear Industry, Garmisch-Partenkirchen, ASTM STP 1295, 1995, pp. 94–113.
[3] A. Yilmazbayhan, E. Breval, A. Motta, R. Comstock, J. Nucl. Mater. 349 (2006) 265–281.
[4] N. Ni, D. Hudson, J. Wei, P. Wang, S. Lozano-Perez, G.D.W. Smith, J.M. Sykes, S.S. Yardley, K.L. Moore, S. Lyon, R. Cottis, M. Preuss, C.R.M. Grovernor, Acta Mater. 60 (2012) 7132–7149.
[5] P. Bossis, G. Lelievre, P. Barberis, X. Iltis, F. Lefebvre, in: Twelfth International Symposium on Zirconium in the Nuclear Industry, Toronto, ASTM STP 1354, 2000, p. 918.
[6] C. Proff, S. Abolhassani, C. Lemaignan, J. Nucl. Mater. 432 (2013) 222–238.
[7] M. Oskarsson, E. Ahlberg, K. Pettersson, J. Nucl. Mater. 295 (2001) 97–108.
[8] A.T. Motta, M.J.G. Da Silva, A. Yilmazbayhan, R.J. Comstock, Z. Cai, B. Lai, in: 15th International Symposium on Zr in the Nuclear Industry, Sunriver, OR, United States, American Society for Testing and Materials ASTM STP 1505, 2009, pp. 486–506.
[9] P. Tejland, H.-O. Andren, J. Nucl. Mater. 430 (2012) 64–74.
[10] Z. Zhao, M. Blat-Yrieix, J.-P. Morniroli, A. Legris, L. Thuinet, Y. Kihn, A. Ambard, L. Legras, J. ASTM Int. 5 (3) (2011) JAI101161.
[11] M. Furuta, J. Nucl. Mater. 95 (1980) 303–306.
[12] B. Hutchinson, B. Lehtinen, M. Limbäck, M. Dahlbäck, in: 15th International Symposium on Zr in the Nuclear Industry, Sunriver, OR, United States, American Society for Testing and Materials ASTM STP 1505, 2009, pp. 269–284.
[13] Y. Dong, A.T. Motta, E.A. Marquis, J. Nucl. Mater. 442 (2013) 270–281.
[14] B. de Gabory, A.T. Motta, Structure of Zircaloy 4 Oxides Formed during Autoclave Corrosion, ANS LWR Fuel Performance Meeting, TopFuel 2013, September 2013, Charlotte, NC, Paper #8584.
[15] X. Iltis, H. Michel, J. Alloy. Compd. 177 (1991) 71–82.
[16] D. Pecheur, F. Lefebvre, A.T. Motta, C. Lemaignan, J.-F. Wadier, J. Nucl. Mater. 189 (1992) 2318–2332.
[17] A. Couet, A.T. Motta, R.J. Comstock, Effect of alloying elements on hydrogen pickup in zirconium alloys, in: 17th International Symposium on Zirconium in the Nuclear Industry, Hyderabad, India, ASTM STP, 2014, pp. 1–33.
[18] D. Hudson, G.D.W. Smith, Scr. Mater. 61 (2009) 411–414.